Error-Tolerant Geometric Quantum Control for Logical Qubits with Minimal Resources

Tao Chen,[1,2] Zheng-Yuan Xue,[2,3,*] and Z.D. Wang[1,3,†]

[1] *Guangdong-Hong Kong Joint Laboratory of Quantum Matter, Department of Physics, and HKU-UCAS Joint Institute for Theoretical and Computational Physics at Hong Kong, The University of Hong Kong, Pokfulam Road, Hong Kong, China*

[2] *Guangdong Provincial Key Laboratory of Quantum Engineering and Quantum Materials, and School of Physics and Telecommunication Engineering, South China Normal University, Guangzhou 510006, China*

[3] *Guangdong-Hong Kong Joint Laboratory of Quantum Matter, and Frontier Research Institute for Physics, South China Normal University, Guangzhou 510006, China*

(Received 16 December 2021; revised 25 March 2022; accepted 27 May 2022; published 26 July 2022)

Geometric quantum computation offers a practical strategy toward robust quantum computation due to its inherent error tolerance. However, the rigorous geometric conditions lead to complex and/or error-disturbed quantum controls, especially for logical qubits that involve more physical qubits, whose error tolerance is effective in principle, but their experimental demonstration is still demanding. Thus, how to best simplify the needed control and manifest its full advantage has become the key to widespread applications of geometric quantum computation. Here we propose a fast and robust geometric scheme, with decoherence-free subspace encoding, and present its physical implementation on superconducting quantum circuits, where we only utilize the experimentally demonstrated parametrically tunable coupling to achieve high-fidelity geometric control over logical qubits. Numerical simulation verifies that it can efficiently combine the error tolerance from both the geometric phase and logical-qubit encoding, displaying our gate-performance superiority over the conventional dynamical one without encoding, in terms of both gate fidelity and robustness. Therefore, our scheme can consolidate both error suppression methods for logical-qubit control, which sheds light on the future large-scale quantum computation.

DOI: 10.1103/PhysRevApplied.18.014062

I. INTRODUCTION

The superiority of quantum computation over classical computation essentially lies in the superposition and entanglement of quantum systems [1]. But an inescapable truth is that the influence of environment-induced decoherence and inaccurate control on a quantum system will greatly limit the performance of quantum gates, which are the building blocks for executing quantum computation, thus revealing the necessity for exploring a method to combat both decoherence and control errors, especially for future large-scale quantum circuits. Geometric phases [2–5], due to their inherent error-tolerant feature, have become critical elements for realizing high-fidelity and robust quantum controls. However, for adiabatic geometric quantum computation (GQC) [6–10], due to the long evolution time needed to satisfy the adiabatic conditions, the resulting gate fidelities are relatively low, despite indeed being more robust against control errors.

Recently, GQC [11–17] based on nonadiabatic geometric phases [4,5] has been proposed to implement robust and high-fidelity quantum gates, which eliminate the restriction of slow evolution. Remarkably, experimental demonstrations for elementary geometric quantum gates have also been achieved on various systems, such as trapped ions [18,19], NMR [20–23], superconducting quantum circuits [24–30], nitrogen-vacancy centers [31–36], etc. Meanwhile, to further consolidate the geometric robustness, many efforts have been made to make GQC more compatible with various optimal-control techniques, including the composite pulse [37,38], dynamical decoupling [39,40], time-optimal control [41], path optimization [42], etc. Nonetheless, the rigorous geometric conditions lead to complex and error-disturbed quantum controls, so that existing GQC is favorable merely for a certain kind of control error. Thus, it is still quite challenging to demonstrate the full error-tolerant advantages for GQC.

Besides control errors, environmental-induced decoherence is another central obstacle in realizing GQC. Methods based on decoherence-free subspace (DFS) encoding [43–46] can utilize the symmetry structure of the

*zyxue83@163.com
†zwang@hku.hk

interaction between the qubit system and its environment to effectively suppress the effect of collective dephasing, which is the major source of decoherence in the quantum system. To this end, the proposed geometric schemes [47–54] under the protection of DFS encoding aim to achieve the combination of geometric error-tolerant features and decoherence resilience of the encoding. However, due to more involved physical qubits, more error sources are introduced too, such that the logical-qubit manipulation becomes complicated and fails to achieve the desired gate performance under hybrid protection in subsequent experimental demonstration.

Here we aim to solve the two aforementioned key problems in GQC: (i) to best simplify the geometric control in order to manifest GQC to its full advantage; (ii) to make GQC more compatible with the protection of DFS encoding. To this end, from a general approach to construct a geometric quantum gate, we propose an improved geometric scheme that can shorten the operation time and possesses the robustness advantage beyond the conventional dynamical scheme. In addition, with the pursuit of a minimal number of physical qubits, we merely utilize parametrically tunable coupling between a transmon and a microwave resonator to achieve high-fidelity geometric control for DFS logical qubits on the superconducting quantum circuit. Our scheme does not require an additional auxiliary level or qubit, and can thus avoid introducing more error sources. Numerical simulation verifies that our scheme can fully consolidate the hybrid-protection capabilities from both the geometric phase and the encoding, by displaying absolute error-tolerant advantages over the dynamical gates without encoding, in terms of both the frequency-drift error and decoherence, which are the main error sources for superconducting quantum circuits. Therefore, our scheme shows the prospect of GQC with logical-qubit encoding that is inevitable in future fault-tolerant quantum computation.

II. A GENERAL SCHEME FOR GEOMETRIC GATES

We first consider a general two-level quantum system that consists of a ground state $|0\rangle = (1,0)^{\dagger}$ and an excited state $|1\rangle = (0,1)^{\dagger}$, as shown in Fig. 1(a). Its arbitrary quantum control can be realized by a microwave drive, as described by the Hamiltonian (assuming that $\hbar = 1$ here and hereafter)

$$\mathcal{H}(t) = \tfrac{1}{2}\mathbf{B}(t)\cdot\boldsymbol{\sigma}, \tag{1}$$

where the control field $\mathbf{B}(t)$ has three directions, which are $B_x = \Omega(t)\cos\phi(t)$, $B_y = \Omega(t)\sin\phi(t)$, and $B_z = -\Delta(t)$; $\boldsymbol{\sigma} = (\sigma_x, \sigma_y, \sigma_z)$ are the Pauli matrices; $\Omega(t)$ and $\phi(t)$ are the time-dependent driving amplitude and phase of the microwave field; and $\Delta(t)$

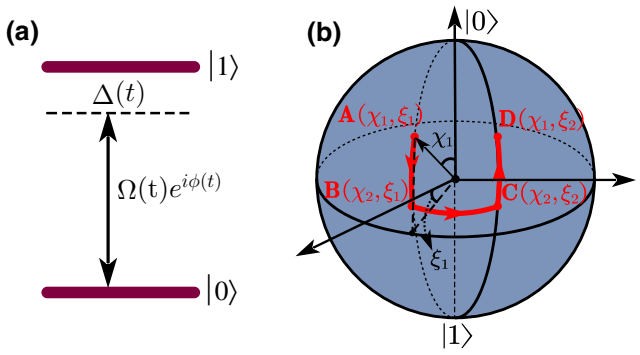

FIG. 1. (a) A simple two-level coupling structure driven by a microwave field. (b) Illustration of a U-shaped geometric evolution path $\mathbf{A} \to \mathbf{B} \to \mathbf{C} \to \mathbf{D}$ of state $|\Psi_0(t)\rangle$ on a Bloch sphere.

is the time-dependent detuning. There is a pair of orthogonal evolution states $|\Psi_i(t)\rangle = e^{if_i(t)}|\psi_i(t)\rangle$ with $i = 0, 1$, $|\psi_0(t)\rangle = \cos(\chi(t)/2)|0\rangle + \sin(\chi(t)/2)e^{i\xi(t)}|1\rangle$ and $|\psi_1(t)\rangle = \sin(\chi(t)/2)e^{-i\xi(t)}|0\rangle - \cos(\chi(t)/2)|1\rangle$, where the phase factor $f_i(t)$ is a global phase of $|\Psi_i(t)\rangle$, and $\chi(t)$ and $\xi(t)$ represent the time-dependent change of polar and azimuth angles of the state vector on a Bloch sphere, as shown in Fig. 1(b). Utilizing the Schrödinger equation as $i|\dot{\Psi}_i(t)\rangle = \mathcal{H}(t)|\Psi_i(t)\rangle$, we solve for

$$\begin{aligned}\dot{\chi}(t) &= -B_x\sin\xi(t) + B_y\cos\xi(t),\\ \dot{\xi}(t) &= -\Delta(t) - \cot\chi(t)[B_x\cos\xi(t) + B_y\sin\xi(t)],\end{aligned} \tag{2}$$

thereby determining the dependence of evolution details of state $|\Psi_i(t)\rangle$ and the control parameters of $\mathcal{H}(t)$. Besides, after a time period τ, accumulated global phase $f_0(\tau) = -f_1(\tau) = \gamma$ includes the dynamical part $\gamma_d = -\int_0^{\tau}\langle\Psi_i(t)|\mathcal{H}(t)|\Psi_i(t)\rangle dt$ and the geometric part

$$\gamma_g = \gamma - \gamma_d = -\frac{1}{2}\int_0^{\tau}\dot{\xi}(t)[1-\cos\chi(t)]dt, \tag{3}$$

where the geometric nature [4,5] of γ_g comes from the fact that it is given by half of the solid angle enclosed by the noncyclic evolution path and its geodesic connecting the initial point $[\chi(0), \xi(0)]$ and the final point $[\chi(\tau), \xi(\tau)]$. In this way, we can determine the pure geometric property of the evolution process by designing state parameters $\dot{\xi}(t)\sin^2\chi(t) = -\Delta(t)$ to meet $\gamma_d = 0$. Thus, substituting this geometric condition into Eq. (2), we can use the solved relations

$$B_x = -\dot{\xi}(t)\sin\chi(t)\cos\chi(t)\cos\xi(t) - \dot{\chi}(t)\sin\xi(t), \tag{4a}$$

$$B_y = -\dot{\xi}(t)\sin\chi(t)\cos\chi(t)\sin\xi(t) + \dot{\chi}(t)\cos\xi(t), \tag{4b}$$

$$B_z = -\dot{\xi}(t)\sin^2\chi(t) \tag{4c}$$

to reversely fix the control parameters of Hamiltonian $\mathcal{H}(t)$.

After an evolution period τ, two evolution states undergo a change as $|\Psi_i(0)\rangle \to |\Psi_i(\tau)\rangle = e^{(-1)^i i\gamma_g}|\psi_i(t)\rangle$, and the associated evolution operator

$$\begin{aligned} U(\tau,0) &= e^{i\gamma}|\psi_0(\tau)\rangle\langle\psi_0(0)| + e^{-i\gamma}|\psi_1(\tau)\rangle\langle\psi_1(0)| \\ &= \begin{pmatrix} (c_{\gamma'}c_{\chi_-} + is_{\gamma'}c_{\chi_+})e^{-i\xi_-} & (-c_{\gamma'}s_{\chi_-} + is_{\gamma'}s_{\chi_+})e^{-i\xi_+} \\ (c_{\gamma'}s_{\chi_-} + is_{\gamma'}s_{\chi_+})e^{i\xi_+} & (c_{\gamma'}c_{\chi_-} - is_{\gamma'}c_{\chi_+})e^{i\xi_-} \end{pmatrix} \end{aligned} \tag{5}$$

can be obtained, where $c_j = \cos j$, $s_j = \sin j$, $p_\pm = [p(\tau) \pm p(0)]/2$, and $\gamma' = \gamma_g + \xi_-$. Therefore, arbitrary geometric gate types are realized by setting the boundary values of parameters $\chi(t)$ and $\xi(t)$. More importantly, time-dependent shapes of parameters $\chi(t)$ and $\xi(t)$ can also be engineered to determine geometric schemes under different evolution processes. Benefiting from it, we then work to implement an improved geometric scheme that can be better compatible with DFS encoding while holding high fidelity and error-tolerant features.

III. AN IMPROVED CONSTRUCTION OF GEOMETRIC GATES

Based on the above general geometric framework, we can set time-dependent shapes of parameters $\chi(t)$ and $\xi(t)$ to realize different geometric evolution processes. We here design a geometric scheme based on a "U-shaped" evolution path with state parameters $[\chi(t), \xi(t)]$ as

$$\chi(0) = \chi_1 \rightsquigarrow \chi(\tau_1) = \chi_2 \to \chi(\tau_2) = \chi_2 \rightsquigarrow \chi(\tau) = \chi_1, \tag{6a}$$

$$\xi(0) = \xi_1 \to \xi(\tau_1) = \xi_1 \rightsquigarrow \xi(\tau_2) = \xi_2 \to \xi(\tau) = \xi_2, \tag{6b}$$

where the arrows "$\to$" and "$\rightsquigarrow$" indicate whether the parameters $\chi(t)$ and $\xi(t)$ remain constant or change with time during the evolution process, respectively. For example, in the first time segment $t \in [0, \tau_1]$, $\chi(t)$ changes from χ_1 to χ_2, while $\xi(t) = \xi_1$ remains constant. The visualized state-evolution details on a Bloch sphere are shown in Fig. 1(b); that is, start from point $\mathbf{A}(\chi_1, \xi_1)$ and evolve along the longitude line with $\xi(t) = \xi_1$ to point $\mathbf{B}(\chi_2,\xi_1)$ at time τ_1; then evolve along the latitude line with $\chi(t) = \chi_2$ to point $\mathbf{C}(\chi_2, \xi_2)$ at time τ_2; finally, evolve to point $\mathbf{D}(\chi_1, \xi_2)$ along the longitude line with $\xi(t) = \xi_2$ at the final time τ. Therefore, under the above evolution process, according to the parameter-limited relations in Eqs. (4), we can determine the Hamiltonian parameters $\Omega(t)$ and $\phi(t)$ in the three segments $t \in [0, \tau_1]$, $[\tau_1, \tau_2]$ and $[\tau_2, \tau]$ as

$$2\int_0^{\tau_1} \Omega(t)dt = |\chi_2 - \chi_1|, \qquad \phi(t) = \xi_1 + \frac{\pi}{2}, \tag{7a}$$

$$\int_{\tau_1}^{\tau_2} \Omega(t)dt = \frac{1}{2}(\xi_2 - \xi_1)\sin(2\chi_2), \qquad \phi(t) = \xi(t) + \pi, \tag{7b}$$

$$\int_{\tau_2}^{\tau} \Omega(t)dt = |\chi_2 - \chi_1|, \qquad \phi(t) = \xi_2 - \frac{\pi}{2}, \tag{7c}$$

respectively, with detuning $\Delta(t) = 0, -\Omega(t)\tan\chi_2, 0$, where $\xi(t) = \xi_1 + \int_{\tau_1}^{t}\Omega(t')dt'/[2\sin(2\chi_2)]$. This is the case of $\chi_2 > \chi_1$, and when $\chi_2 < \chi_1$, parameter $\phi(t)$ in the time segments $t \in [0, \tau_1]$ and $t \in [\tau_2, \tau]$ should be changed to $\xi_1 - \pi/2$ and $\xi_2 + \pi/2$, respectively. Note that the pulse shape here can be arbitrary, providing its pulse area is as prescribed. The final evolution operator is written as

$$\begin{aligned} U(\tau) &= U(\tau,\tau_2)U(\tau_2,\tau_1)U(\tau_1,0) \\ &= \begin{pmatrix} (c_{\gamma'} + is_{\gamma'}c_{\chi_1})e^{-i\xi_-} & is_{\gamma'}s_{\chi_1}e^{-i\xi_+} \\ is_{\gamma'}s_{\chi_1}e^{i\xi_+} & (c_{\gamma'} - is_{\gamma'}c_{\chi_1})e^{i\xi_-} \end{pmatrix}, \end{aligned} \tag{8}$$

where $\gamma' = \gamma_g + \xi_-$ with the accumulated geometric phase in this evolution process being $\gamma_g = -(\xi_2 - \xi_1)(1 - \cos\chi_2)/2$. We find that the geometric Hadamard gate U_H^g, phase gate U_S^g, and $\pi/8$ gate U_T^g, corresponding to the matrices

$$\begin{aligned} U_H^g &= \frac{1}{\sqrt{2}}\begin{pmatrix} 1 & 1 \\ 1 & -1 \end{pmatrix}, \quad U_S^g = \begin{pmatrix} 1 & 0 \\ 0 & e^{i\pi/2} \end{pmatrix}, \\ U_T^g &= \begin{pmatrix} 1 & 0 \\ 0 & e^{i\pi/4} \end{pmatrix}, \end{aligned} \tag{9}$$

can all be realized by setting $\{\gamma' = \pi/4, \xi_2 - \xi_1 = 3\pi, \chi_1 = \pi/2\}$, $\{\gamma' = \pi, \xi_2 - \xi_1 = 5\pi/2\}$, and $\{\gamma' = \pi, \xi_2 - \xi_1 = 9\pi/4\}$, respectively, which constitute a universal set for single-qubit gates [1].

IV. THE PERFORMANCE SUPERIORITY OF GEOMETRIC GATES

Next, we continue to verify the advantages of our geometric scheme over the conventional dynamical one (for details, see Appendix A), in terms of gate performance.

Firstly, the needed gate-operation time is an important factor for gate performance and determines the impact from environment-induced decoherence. From the comparison results listed in Fig. 2(a), we find that the time we consume to construct a geometric gate is less than that of the dynamical counterpart, where $\Omega(t) = \Omega$ is set to be constant for simplicity. Secondly, we also consider the driving amplitude and detuning errors induced by the imperfect control, in the form of $(1+\epsilon)\Omega$ and $\Delta(t) + \eta\Omega$. We use the formula $F_{\epsilon,\eta} = \mathrm{Tr}(U^\dagger U_{\epsilon,\eta})/\mathrm{Tr}(U^\dagger U)$ to evaluate gate robustness in the presence of control errors, in which U and $U_{\epsilon,\eta}$ are respectively the gate without and with errors. The results of a numerical simulation are shown in Figs. 2(b)–2(g), which exhibit the advantage of our scheme in terms of both the gate fidelity and robustness. Finally, it needs to be emphasized that the time-dependent pulse can also be applicable to our geometric scheme and exhibits the same effect as above. So far, our simulation starts with a general two-level structure that can be easily addressed in realistic quantum systems, such as trapped ions, the superconducting quantum circuit, the nitrogen-vacancy center, etc.; thus, it can be expected that our geometric scheme can also exhibit error-tolerant features. In the following, we verify this in a scalable superconducting system.

(a)	Hadamard Gate	Phase Gate	$\pi/8$ Gate
Geometric Gates	$0.6\pi/\Omega$	$1.2\pi/\Omega$	$0.92\pi/\Omega$
Dynamical Gates	$1.5\pi/\Omega$	$1.5\pi/\Omega$	$1.25\pi/\Omega$

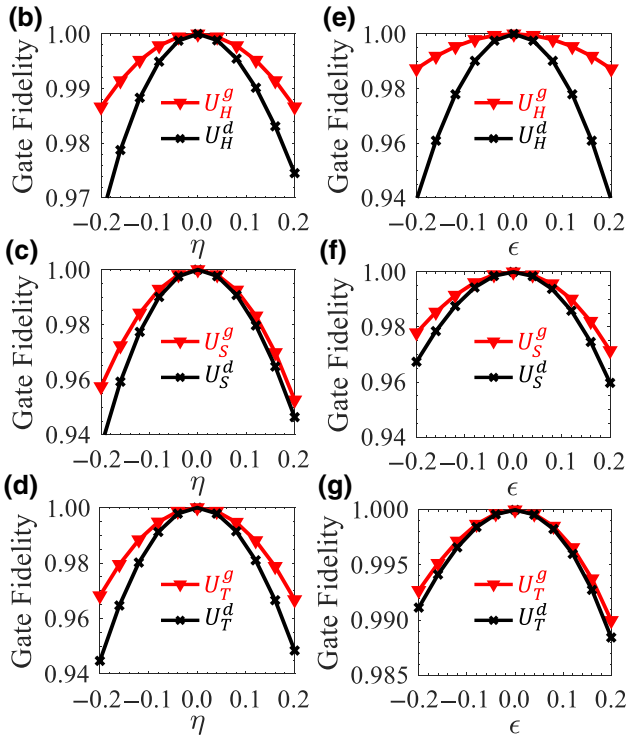

FIG. 2. Comparison of our geometric gates and the conventional dynamical counterparts in terms of (a) the gate time and (b)–(g) robustness.

V. IMPLEMENTATION WITH ENCODING

For the superconducting transmon qubit, a common method used to achieve precise control of a single qubit is to apply the derivative removal by adiabatic gate (DRAG) correction technology [55,56] to suppress the computational basis leakage caused by the transmon's anharmonicity. However, it is necessary to set the drive to be time dependent there, resulting in a longer gate time than the square pulse, so the decoherence effect and loss of gate robustness will also increase significantly. Therefore, here we propose implementing our universal geometric gates under the protection of DFS encoding on a two-dimensional (2D) transmon-resonator lattice as shown in Fig. 3(a), which can combine the error-tolerant features of our geometric scheme and the decoherence resilience of DFS encoding. With the pursuit of a minimal number of physical qubits and without any additional auxiliary, here we only use a capacitively coupled transmon Q_1 and microwave resonator R_a to encode a DFS logical qubit; thus, there will exist a two-dimensional DFS $S_1 = \{|10\rangle, |01\rangle\}$, where the encoded computational bases are denoted as $|0\rangle_L = |10\rangle$ and $|1\rangle_L = |01\rangle$ with $|mn\rangle = |m\rangle_1 \otimes |n\rangle_a$. For the parametrically tunable coupling [57,58] between a transmon Q_1 and a fixed-frequency microwave resonator R_a, it is obtained by introducing an additional qubit-frequency driving for transmon Q_1, in the form $\omega_{q_1}(t) = \omega_{q_1} + \varepsilon_1 \sin(\nu_1 t + \varphi_1)$, which can be experimentally achieved by biasing the transmon with an ac magnetic flux. The energy level transition structure of the above interaction Hamiltonian is shown in Fig. 3(b);

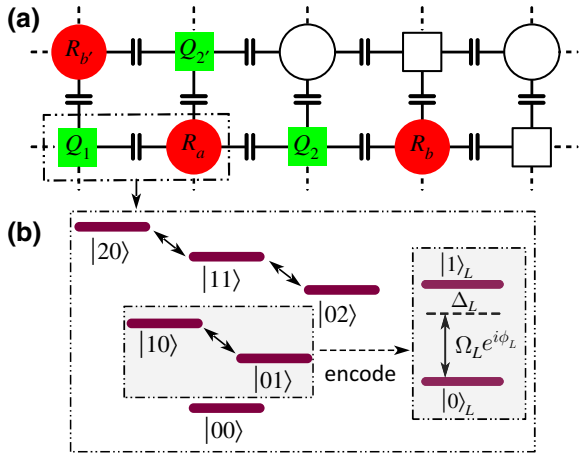

FIG. 3. (a) A scalable 2D superconducting transmon-resonator lattice. (b) Energy level diagram of the capacitive coupling of a single transmon and a microwave resonator, where the single-excitation subspace $\{|10\rangle, |01\rangle\}$ as an effective two-level structure can encode a single-logical-qubit DFS.

there is naturally no leakage from DFS S_1 to the multiexcitation subspaces, and thus no additional correction for the computational basis leakage is required. Furthermore, in the DFS representation $\{|0\rangle_L, |1\rangle_L\}$, the obtained effective Hamiltonian is of the same form as Eq. (1) (for the derivation details, see Appendix B); thus, arbitrary single-logical-qubit geometric gates, as in Eq. (8), can be realized under the geometric parameter constraints in Eqs. (7).

We take the Hadamard gate $U^g_{H_L}$, phase gate $U^g_{S_L}$, and $\pi/8$ gate $U^g_{T_L}$ as typical examples to numerically show the performance of these universal single-logical-qubit geometric gates by using the quantum master equation, where the simulation details are given in Appendix E. According to state-of-the-art technology in the experiments [59–61], here we set a conservative parameter region (for details, see Appendix F), in which the transmon energy-relaxation time and its pure dephasing time are $T_1 = T_\phi = T_{\rm tran} = 40\ \mu$s, and the resonator energy-relaxation time is $T_{\rm res} = 150\ \mu$s. The coupling strength between transmon Q_1 and resonator R_a is $g_{1a} = 2\pi \times 20$ MHz with the anharmonicity of Q_1 $\alpha_1 = 2\pi \times 240$ MHz. At a frequency difference between Q_1 and R_a of $\Delta_1 = 2\pi \times 180$ MHz, the gate fidelities of the geometric Hadamard gate, phase gate, and $\pi/8$ gate can be as high as 99.95%, 99.92%, and 99.94% by adjusting $\beta_1 = \varepsilon_1/\nu_1 \approx 2.1$, respectively. Besides, the flux noise [62–64] will inevitably be introduced during flux modulation for realizing parametrically tunable coupling. Thus, the frequency drift ($\omega_{q_1} \to \omega_{q_1} + \delta_1$) of a working transmon induced by the flux noise can be up to a few of megahertz, which together with decoherence (including qubit energy relaxation and pure dephasing) is regarded as the main source of gate error in superconducting systems. In Figs. 4(a) and 4(b), we plot the gate fidelity as a function of shorter coherence time $T_{\rm tran}$ and frequency-drift quantity δ_1, respectively, where the shorter coherence time $T_{\rm tran}$ characterizes more decoherence effects. These results demonstrate that, although more physical resources are involved, our geometric encoding scheme still has a stronger error robustness than the conventional dynamical gates, which are realized by applying DRAG correction on a single transmon (Q_1) under the same parameter settings. In addition, our geometric encoding scheme can be insensitive to the influence of decoherence due to the shorter gate-operation time and the coherence protection from encoding. Remarkably, we further consider the joint influence of qubit-frequency drift and decoherence, with the results shown in Figs. 4(c) and 4(d) powerfully verifying the error-tolerant features of our scheme.

Furthermore, for the previous geometric scheme [16] based on a "single-looped" geometric evolution process that can also be engineered by applying our general geometric framework in Sec. II, due to the requirement of a longer gate-operation time, the gate fidelities will suffer more losses from decoherence in the superconducting transmon-resonator system. Thus, unlike

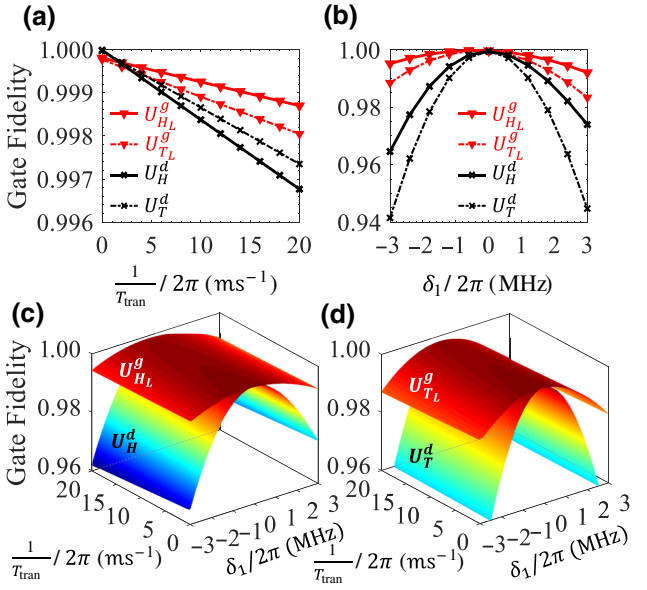

FIG. 4. Performance comparisons for our geometric gates under the protection of DFS encoding and the dynamical gates realized on a single transmon under the effects of (a) decoherence and (b) qubit-frequency drift, which are regarded as the main sources of gate errors in superconducting quantum circuits, where the decoherence effect is characterized by coherence time $T_{\rm tran}$. Comparison of comprehensive effects for the (c) Hadamard gate and (d) $\pi/8$ gate. Note that the performance of the phase gate is similar to that of the $\pi/8$ gate and thus not mentioned here and hereafter.

our current U-shaped geometric scheme, the combination of the single-looped geometric scheme and DFS encoding fails to thoroughly exploit the desired hybrid protection, as discussed in detail in Appendix C.

Next, we extend our geometric approach to the situation of two logical qubits, as shown in Fig. 3(a), and prove the overall gate-performance advantages compared to the "two-physical-qubit dynamical gate" realized by tunable coupling between only two transmons. We continue to utilize a transmon Q_2 and a microwave resonator R_b on the same chain as the first logical qubit to encode the second logical qubit; thus, there exists a four-dimensional DFS $S_2 = \{|1010\rangle, |1001\rangle, |0110\rangle, |0101\rangle\} = \{|00\rangle_L, |01\rangle_L, |10\rangle_L, |11\rangle_L\}$ for two-logical qubits. In the same way (see Appendix D for the derivation details), we can efficiently obtain the two-logical-qubit controlled-phase gate

$$U^g_{\rm CP}(\zeta) = \mathrm{diag}\{1, 1, e^{i\zeta}, 1\} \tag{10}$$

with ζ being a geometric phase. In the following, we evaluate the performance of $U^g_{\rm CP}(\pi/2)$ by utilizing the master equation, where the influence of high-order oscillating terms and decoherence of transmons (Q_1, Q_2) and

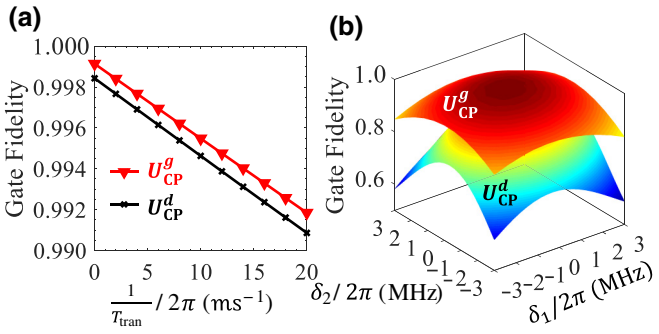

FIG. 5. Performance comparisons for a two-logical-qubit controlled-phase geometric gate and a two-physical-qubit dynamical counterpart under the effects of (a) shorter coherence time and (b) qubit-frequency drifts ($\omega_{q_1} \to \omega_{q_1} + \delta_1$ and $\omega_{q_2} \to \omega_{q_2} + \delta_2$) of two transmons Q_1 and Q_2.

microwave resonators (R_a, R_b) are all taken into consideration. Here, we set the coupling strength $g_{a2} = 2\pi \times 8$ MHz, and anharmonicity of the other transmon Q_2 as $\alpha_2 = 2\pi \times 220$ MHz. When the frequency difference between Q_2 and R_a is $\Delta_2 = 2\pi \times 500$ MHz and the driving parameter $\beta_2 = \varepsilon_2/\nu_2 \approx 1.2$, we can simulate that the fidelity of a two-logical-qubit controlled-phase geometric gate up to 99.76% under the coherence time $T_1 = T_\phi = T_{\text{tran}} = 40$ μs and $T_{\text{res}} = 150$ μs; this result is comparable to the fidelity with 99.68% of a two-physical-qubit dynamical gate $U_{\text{CP}}^{d}(\pi/2)$ realized only on transmons Q_1 and Q_2 under the same parameter settings. Furthermore, in Figs. 5(a) and 5(b), the numerical results indicate that, under the influence of a shorter coherence time and qubit-frequency drifts, our controlled-phase geometric gate with encoding shows a stronger error-tolerant feature over the two-physical-qubit dynamical gate.

VI. CONCLUSION

In summary, we propose a fast and robust geometric scheme based on a simple two-level structure. And we merely utilize tunable coupling between a transmon and a microwave resonator to achieve high-fidelity geometric logical control in superconducting quantum circuits. Furthermore, from the numerical results, we can obviously find that, under hybrid protection of the geometric phase and DFS encoding, our single- and two-logical-qubit geometric gates can all show higher fidelity and greater robustness than the dynamical ones without DFS encoding. Therefore, all of these sufficiently demonstrate that our scheme paves the way for achieving robust GQC.

ACKNOWLEDGMENTS

The authors thank Z. Hua and S. Li for helpful discussions. This work is supported by the Key-Area Research and Development Program of GuangDong Province (Grant No. 2019B030330001), the CRF (No. C6009-20G) of Hong Kong, the National Natural Science Foundation of China (Grant No. 11874156), and the Science and Technology Program of Guangzhou (Grant No. 2019050001).

APPENDIX A: DYNAMICAL QUANTUM GATES

A conventional dynamical quantum gate [59,65], mentioned in the main text, can be realized by a resonant two-level drive. The corresponding Hamiltonian is as given in Eq. (1) with $\Delta(t) = 0$, in which the driving phase $\phi(t) = \phi_d$ is a constant to ensure that there is no accumulation of geometric phase. In this way, the dynamical Hadamard gate U_H^d, phase gate U_S^d, and $8/\pi$ gate U_T^d are respectively obtained by the operations of $R_x(\pi)R_y(\pi/2)$, $R_y(-\pi/2)R_x(\pi/2)R_y(\pi/2)$, and $R_y(-\pi/2)R_x(\pi/4)R_y(\pi/2)$, where the corresponding operation elements $R_x(\theta)$ and $R_y(\theta)$ are the dynamical X- and Y-axis rotation operations for arbitrary angle $\theta = \int_0^\tau \Omega(t)dt$, which can be done by determining $\phi_d = 0$ and $\pi/2$, respectively.

In addition, in the superconducting physical implementation of single-qubit dynamical gates, the corresponding control field needs to be corrected to $\mathbf{B}_C(t) = \mathbf{B}(t) + \mathbf{B}_D(t)$, in which $\mathbf{B}(t)$ and $\mathbf{B}_D(t) = (-\dot{B}_y + B_z B_x, \dot{B}_x + B_z B_y, 0)/(2\alpha_1)$ are the original and additional DRAG-correcting microwave fields, respectively, where α_1 is the anharmonicity of the working transmon Q_1. Consider the constraint of experimental control and DRAG correction on a single transmon, it is necessary to set a time-dependent pulse shape and ensure that $\Omega(0) = \Omega(\tau) = 0$. In the comparison in the main text, we set $\Omega(t) = \Omega_m \sin(\pi t/\tau)$ as an example for simplicity.

APPENDIX B: TUNABLE TRANSMON-RESONATOR COUPLING

To achieve effective control for the single-logical-qubit states $|0\rangle_L$ ($|10\rangle$) and $|1\rangle_L$ ($|01\rangle$), we can utilize the parametrically tunable coupling between a transmon Q_1 and a fixed-frequency microwave resonator R_a, which is obtained by introducing an additional qubit-frequency driving for transmon Q_1. Moving into the interaction picture, the system Hamiltonian can be written as

$$\begin{aligned}\mathcal{H}_I^1(t) = g_{1a}\{&|10\rangle\langle 01|e^{i\Delta_1 t}e^{-i\beta_1\cos(\nu_1 t+\varphi_1)} \\ &+ \sqrt{2}|20\rangle\langle 11|e^{i(\Delta_1-\alpha_1)t}e^{-i\beta_1\cos(\nu_1 t+\varphi_1)} \\ &+ \sqrt{2}|11\rangle\langle 02|e^{i\Delta_1 t}e^{-i\beta_1\cos(\nu_1 t+\varphi_1)}\} + \text{H.c.},\end{aligned} \tag{B1}$$

where $\beta_1 = \varepsilon_1/\nu_1$; g_{1a} and Δ_1 are the coupling strength and the difference in the transition frequency between transmon Q_1 and microwave resonator R_a; α_n is the intrinsic anharmonicity of transmon Q_n. The energy level transition structure corresponding to Hamiltonian $\mathcal{H}_I^1(t)$ is

shown in Fig. 3(b); we obviously find that the single-excitation subspace $\{|10\rangle, |01\rangle\}$ can form an effective two-level structure. Furthermore, when we encode the computational basis into DFS S_1, there is naturally no leakage from S_1 to the multiexcitation subspaces. Therefore, unlike the control in a single transmon, our encoding method is not limited by the transmon's anharmonicity, and also does not rely strictly on a time-dependent pulse shape for correcting the computational basis leakage.

Here we utilize the Jacobi-Anger identity to expand e-index terms in Eq. (B1), and modulate the qubit-driving frequency ν_1 to satisfy $\Delta_1 - \nu_1 = -(\Delta_L + \mu)$ with $|\Delta_L + \mu| \ll \{\Delta_1, \nu_1\}$. Then, by neglecting the high-order oscillating terms, and applying the unitary transformation with the transformation matrix $U_R(t) = \exp[-i(\Delta_L/2)\sigma_z^L t]$, the final effective Hamiltonian can be obtained as

$$\mathcal{H}_L(t) = \tfrac{1}{2}\Omega_L[\cos\phi_L(t)\sigma_x^L + \sin\phi_L(t)\sigma_y^L] - \tfrac{1}{2}\Delta_L\sigma_z^L, \tag{B2}$$

where $\sigma_{x,y,z}^L$ are the Pauli operators in the single-logical-qubit subspace $\{|0\rangle_L, |1\rangle_L\}$; the coupling strength $\Omega_L = 2J_1(\beta_1)g_{1a}$ with $J_1(\beta_1)$ a Bessel function of the first kind; and the relative phase $\phi_L(t) = \mu t + \varphi_1 + \pi/2$. The above Hamiltonian form is equivalent to $\mathcal{H}(t)$ in Eq. (1) under the DFS representation $\{|0\rangle_L, |1\rangle_L\}$.

APPENDIX C: SINGLE-LOOPED GEOMETRIC QUANTUM GATES

Based on our general approach to construct geometric gates in the main text, we can also design the time-dependent shapes of state parameters $\chi(t)$ and $\xi(t)$ as

$$\chi(0) = \chi \rightsquigarrow \chi(\tau_1) = 0 \rightsquigarrow \chi(\tau_2) = \pi \rightsquigarrow \chi(\tau) = \chi, \tag{C1a}$$

$$\xi(0) = \xi_1 \rightsquigarrow \xi(\tau_1) = \xi_2 \rightarrow \xi(\tau_2) = \xi_2 \rightsquigarrow \xi(\tau) = \xi_1, \tag{C1b}$$

to realize a "single-looped" geometric evolution process [16], where the arrows "$\rightarrow$" and "$\rightsquigarrow$" indicate whether the parameters $\chi(t)$ and $\xi(t)$ remain constant or change with time during the evolution process, respectively; in addition, for the change of ξ_1 in the first time segment $t \in [0, \tau_1]$, just mutate to ξ_2 at moment τ_1, and keep ξ_1 unchanged at other times in the time segment $t \in [0, \tau_1]$; likewise, for the change of ξ_2 in the third time segment $t \in [\tau_2, \tau]$, just mutate to ξ_1 at moment τ_2, and keep ξ_1 unchanged for the rest of the time. The details of state evolution on a Bloch sphere are as follows: start from point (χ, ξ_1) and evolve along the longitude line to the north pole $(0, \xi_2)$ at time τ_1; then evolve along the longitude line to the south pole (π, ξ_2) at time τ_2; finally, back to the initial point (χ, ξ_1) along the longitude line at the final time τ, where $\xi(t)$ remains unchanged on the longitude line, only changing from ξ_1 to ξ_2 and from ξ_2 back to ξ_1 at the north pole and south pole, i.e., the intermediate time points τ_1 and τ_2, respectively.

In the same way, under the above single-looped evolution process, according to the parameter-limited relations in Eqs. (4), we can also determine the Hamiltonian parameters $\Omega(t)$ and $\phi(t)$ in the three segments $t \in [0, \tau_1]$, $[\tau_1, \tau_2]$, and $[\tau_2, \tau]$ as $\int_0^{\tau_1} \Omega(t)dt = \chi$, $\int_{\tau_1}^{\tau_2} \Omega(t)dt = \pi$, and $\int_{\tau_2}^{\tau} \Omega(t)dt = \pi - \chi$; and $\phi(t) = \xi_1 - \pi/2$, $\phi(t) = \xi_1 + \gamma + \pi/2$, and $\phi(t) = \xi_1 - \pi/2$, respectively, with $\gamma = \xi_2 - \xi_1$ and constant detuning $\Delta(t) \equiv 0$. Substituting Eqs. (C1) into Eq. (5), or directly solving the evolution operator corresponding to the Hamiltonian parameters, arbitrary single-looped geometric gates can be obtained. Thus we applied our general geometric framework in Sec. II to realize the previous single-looped geometric scheme [16].

We now turn to implementing the above single-looped geometric scheme with DFS encoding in the transmon-resonator system [that is, start from effective Hamiltonian $\mathcal{H}_L(t)$ in Eq. (B2)], and compare its gate performance with our geometric scheme based on a U-shaped evolution path. Obviously, single-looped geometric operations under encoding all require $2\pi/\Omega_L$ gate time, so it can be expected that their gate fidelities will suffer more losses from decoherence in realistic quantum systems. In the following numerical simulation, since the performance of the phase gate is similar to that of the $\pi/8$ gate, we take the single-looped geometric Hadamard gate $U_{H_L}^{g'}$ and the $\pi/8$ gate $U_{T_L}^{g'}$ as two typical examples to show the result of hybrid protection from geometric phase and encoding, and also compare it with our U-shaped geometric encoding scheme and the conventional dynamical one without encoding.

Unfortunately, since a longer gate time brings more cumulative influence of decoherence and high-order oscillating terms, under the optimal qubit parameters of $\Delta_1 = 2\pi \times 280$ MHz and $\beta_1 = \varepsilon_1/\nu_1 \approx 2.1$, the simulated fidelities of single-looped $U_{H_L}^{g'}$ and $U_{T_L}^{g'}$ geometric gates are just 99.86% and 99.88%, respectively, which cannot reach above 99.90%. Meanwhile, as shown in Figs. 6(a) and 6(b), when amplifying the decoherence and considering qubit frequency-drift errors that are regarded as the main error sources in the superconducting system, we find that the single-looped geometric gate has better resistance to frequency drift than the conventional dynamical gate without encoding, but it is subject to the destructive effect of decoherence. Therefore, from the joint influence of two key factors, as shown in Figs. 6(c) and 6(d), our U-shaped geometric scheme is a better choice for compatible DFS encoding to obtain high-fidelity and robust quantum gates.

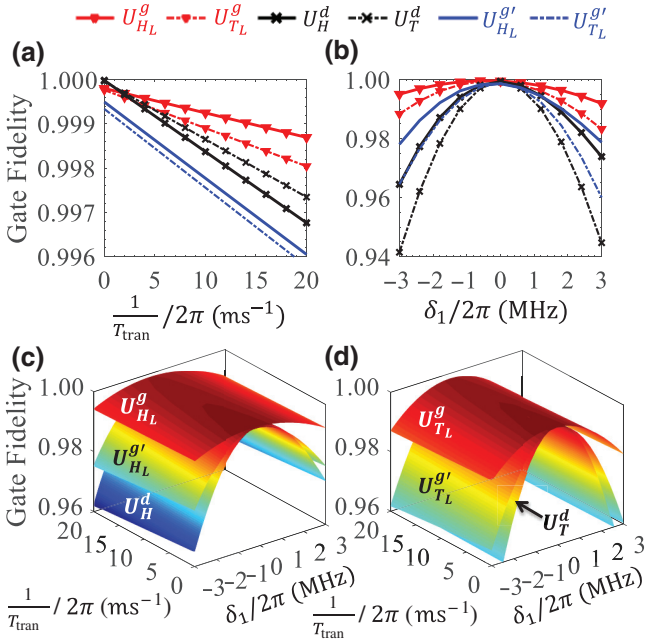

FIG. 6. Performance comparisons for our U-shaped geometric gates and single-looped geometric gates under encoding, and the dynamical gates without encoding, under the effects of (a) decoherence and (b) qubit-frequency drift. Comparison of comprehensive effects for the (c) Hadamard gate and (d) $\pi/8$ gate for different schemes.

APPENDIX D: TWO-LOGICAL-QUBIT GEOMETRIC GATE

As shown in Fig. 3(a), we continue to utilize another transmon Q_2 and a resonator R_b on the same chain as the first logical qubit to encode the second logical qubit. With the general scalability of our encoding scheme, we can also utilize $Q_{2'}$ and $R_{b'}$ in the column direction of a two-dimensional superconducting lattice to encode the second logical qubit. In addition, for arbitrary target control of the two-logical-qubit states, we can realize it by the parametrically tunable coupling between adjacent microwave resonator R_a and transmon Q_2, in which transmon Q_2 is driven by an additional qubit-frequency driving in the form of $\omega_{q_2}(t) = \omega_{q_2} + \varepsilon_2 \sin(\nu_2 t + \varphi_2)$. Thus, the corresponding interaction Hamiltonian can be described as

$$\begin{aligned}\mathcal{H}_I^2(t) = g_{a2}\{&|01\rangle_{a2}\langle 10|e^{i\Delta_2 t}e^{-i\beta_2\cos(\nu_2 t+\varphi_2)} \\ &+ \sqrt{2}|02\rangle_{a2}\langle 11|e^{i(\Delta_2-\alpha_2)t}e^{-i\beta_2\cos(\nu_2 t+\varphi_2)} \\ &+ \sqrt{2}|11\rangle_{a2}\langle 20|e^{i\Delta_2 t}e^{-i\beta_2\cos(\nu_2 t+\varphi_2)}\} + \text{H.c.},\end{aligned} \tag{D1}$$

where $\beta_2 = \varepsilon_2/\nu_2$; g_{a2} and Δ_2 are the coupling strength and the difference in the transition frequency between transmon Q_2 and microwave resonator R_a. The energy level transition structure of the Hamiltonian $\mathcal{H}_I^2(t)$ is similar to Fig. 3(b). But, different from the single-logical-qubit case manipulated in the single-excitation subspace, the manipulation of our two-logical-qubit states need to be implemented in the two-excitation subspace $\{|02\rangle_{a2}, |11\rangle_{a2}\}$ to realize a nontrivial controlled-phase gate. To this end, we here modulate driving frequency ν_2 to satisfy $\Delta_2 - \alpha_2 - \nu_2 = -(\Delta_{L_2} + \upsilon)$ with $|\Delta_{L_2} + \upsilon| \ll \{\Delta_2 - \alpha_3, \nu_2\}$, and apply the unitary transformation; the Hamiltonian mapped into the DFS S_2 representation then reads

$$\begin{aligned}\mathcal{H}_{L_2}(t) = &-\frac{\Delta_{L_2}}{2}(|a\rangle_L\langle a| - |11\rangle_L\langle 11|) \\ &+ \frac{\Omega_{L_2}}{2}(e^{-i\phi_{L_2}(t)}|a\rangle_L\langle 11| + \text{H.c.}),\end{aligned} \tag{D2}$$

where the auxiliary state $|a\rangle_L = |0020\rangle$, and the effective coupling strength and relative phase are $\Omega_{L_2} = 2\sqrt{2}J_1(\beta_2)g_{a2}$ and $\phi_{L_2}(t) = \upsilon t + \varphi_2 + \pi/2$, respectively. For a set of orthogonal evolution states,

$$|\Psi_0^L(t)\rangle = e^{iF_0(t)}\left[\cos\frac{\chi^L(t)}{2}|a\rangle_L + \sin\frac{\chi^L(t)}{2}e^{i\xi^L(t)}|11\rangle_L\right],$$
$$|\Psi_1^L(t)\rangle = e^{iF_1(t)}\left[\sin\frac{\chi^L(t)}{2}e^{-i\xi^L(t)}|a\rangle_L - \cos\frac{\chi^L(t)}{2}|11\rangle_L\right],$$

under the control of $\mathcal{H}_{L_2}(t)$, similar to the derivation process of Eqs. (2)–(7), in addition to meeting the geometric condition, we also need to determine parameter $\chi_1^L = 0$ to ensure that the evolution state $|\Psi_1^L(t)\rangle$ will not leak to the noncomputational subspace at the final moment $t = \tau'$, and accumulate a geometric phase as $\gamma_g = -\xi_2^L(1 - \cos\chi_2^L)/2$ in the two-logical-qubit state $|11\rangle_L$, where we define $\xi_1^L = 0$ for simplicity. Therefore, by engineering the Hamiltonian parameters Ω_{L_2} and $\phi_{L_2}(t)$ in the time segments $t \in [0, \tau_1']$, $[\tau_1', \tau_2']$, and $[\tau_2', \tau']$ as

$$2\Omega_{L_2}\tau_1' = \chi_2^L, \quad \phi_{L_2}(t) = \frac{\pi}{2}, \tag{D3a}$$

$$\Omega_{L_2}(\tau_2' - \tau_1') = \frac{1}{2}\xi_2^L\sin(2\chi_2^L),$$
$$\phi_{L_2}(t) = \pi + \frac{\Omega_{L_2}(t - \tau_1')}{2\sin(2\chi_2^L)}, \tag{D3b}$$

$$\Omega_{L_2}(\tau' - \tau_2') = \chi_2^L, \quad \phi_{L_2}(t) = \xi_2^L - \frac{\pi}{2}, \tag{D3c}$$

respectively, with $\Delta_{L_2} = 0, -\Omega_{L_2}\tan\chi_2^L, 0$; the final evolution operator within the two-logical-qubit DFS S_2 is

$$U_{\text{CP}}^g(\zeta) = \text{diag}\{1, 1, e^{i\zeta}, 1\}, \tag{D4}$$

in which $\zeta = -\gamma_g = \xi_2^L(1 - \cos\chi_2^L)/2$. Note that, for the two-logical-qubit controlled-phase geometric gate $U_{\text{CP}}^g(\pi/2)$ with target phase $\zeta = \pi/2$, parameter χ_2^L (or ξ_2^L)

still has different choices to realize the same gate type at the final time $\tau' = 2[\chi_2^L + \xi_2^L \sin(2\chi_2^L)]/\Omega_{L_2}$, so we determine $\chi_2^L = 0.56\pi$ to gain the least gate-time consumption.

APPENDIX E: QUANTUM MASTER EQUATION AND CALCULATING FIDELITY

The quantum system is inevitably affected by decoherence due to its coupling with the surrounding environment, so we need to consider the effects of decoherence and the neglected high-order oscillating terms simultaneously in our subsequent numerical simulation. The performance of our universal logical-qubit gates can be numerically evaluated by using the quantum master equation [60] as

$$\dot{\rho}_n = -i[\mathcal{H}_I^n(t), \rho_n] + \sum_{n=1,2}\sum_{u=1,\phi}\frac{1}{T_u}\mathcal{L}(X_u^n) + \sum_{w=a,b}\frac{1}{T_{\rm res}}\mathcal{L}(Y_w), \tag{E1}$$

where ρ_n is the density matrix of the quantum system under consideration, $\mathcal{L}(\mathcal{A}) = \mathcal{A}\rho_n\mathcal{A}^\dagger - \frac{1}{2}(\mathcal{A}^\dagger\mathcal{A}\rho_n + \rho_n\mathcal{A}^\dagger\mathcal{A})$ is the Lindblad operator for operator $\mathcal{A}$ with $X_1^n = \sum_{j=0}^{+\infty}\sqrt{j+1}|j\rangle_n\langle j+1|$, $X_\phi^n = \sum_{j=0}^{+\infty} j\,|j\rangle_n\langle j|$ and $Y_w = \sum_{j=0}^{+\infty}\sqrt{j+1}|j\rangle_w\langle j+1|$; $n = 1$ and $n = 2$ correspond to single- and two-logical-qubit cases, respectively. In addition, T_1 and T_ϕ represent the transmon energy-relaxation time and pure dephasing time, respectively; $T_{\rm res}$ is the resonator energy-relaxation time. Since the dephasing time of the resonator is more than an order of magnitude larger than its energy-relaxation time, the dephasing effect is almost negligible and not considered here. According to state-of-the-art technology in the experiments [59–61], we choose a conservative parameter setting with $T_1 = 40\ \mu$s, $T_\phi = 40\ \mu$s, and $T_{\rm res} = 150\ \mu$s, and assume that the influence of the relaxation and dephasing of two transmons is the same as in the main text for convenience, i.e., $T_1 = T_\phi = T_{\rm tran}$.

Therefore, by numerically solving the above quantum master equation, we can obtain the final density matrices ρ_{f1} and ρ_{f2} of single-qubit and two-logical qubits. Note that in our numerical simulation, (i) we consider the influence of high-order oscillating terms and decoherence of all transmons (Q_1, Q_2) and microwave resonators (R_a, R_b) in the case of two-logical qubits; (ii) since the geometric manipulations of single- and two-logical qubits involve only single- and two-excitation subspaces, and it is also numerically verified that other multiexcitation states do not have any influence on gate fidelity, here we consider the lowest three energy levels of transmons and resonators; (iii) our numerical calculation is based on the full Hamiltonians $\mathcal{H}_I^1(t)$ and $\mathcal{H}_I^2(t)$ and does not rely on any further approximation.

We next use the solved density matrix to fully evaluate our implemented geometric quantum gates based on DFS encoding. Thus we can define the gate fidelity of the single-logical qubit as $F_1^G = (1/2\pi)\int_0^{2\pi}\langle\psi_{f_1}|\rho_{f1}|\psi_{f_1}\rangle d\theta_1$, where $|\psi_{f_1}\rangle = U(\tau)|\psi_1\rangle$ is the ideal final state for the general initial state of the single-logical qubit $|\psi_1\rangle = \cos\theta_1|0\rangle_L + \sin\theta_1|1\rangle_L$. In the same way, based on the solved density matrix ρ_{f2}, two-logical-qubit gate fidelity can be defined as $F_{\rm CP}^G = (1/4\pi^2)\int_0^{2\pi}\int_0^{2\pi}\langle\psi_{f_{\rm CP}}|\rho_{f2}|\psi_{f_{\rm CP}}\rangle d\vartheta_1 d\vartheta_2$, where $|\psi_{f_{\rm CP}}\rangle = U_{\rm CP}^g(\pi/2)|\psi_2\rangle$ is the ideal final state for the general initial state of two-logical qubits $|\psi_2\rangle = (\cos\vartheta_1|0\rangle_L + \sin\vartheta_1|1\rangle_L)\otimes(\cos\vartheta_2|0\rangle_L + \sin\vartheta_2|1\rangle_L)$.

APPENDIX F: CONTRIBUTION ANALYSIS OF GATE INFIDELITY

In this appendix we discuss in detail the main sources of gate-infidelity contribution, and find the optimal parameter region for realizing high gate fidelity.

Without considering the error caused by the imperfect control, in addition to the decoherence of the quantum system, the high-order oscillating terms of the original Hamiltonian also contribute to gate infidelity. For the single-logical-qubit case, although the computational bases $\{|0\rangle_L = |10\rangle, |1\rangle_L = |01\rangle\}$ encoded in the DFS do not have the leakage coupling with multiexcitation states (such as $|11\rangle$, $|02\rangle$, $|20\rangle$, etc.), the high-order oscillating terms in the original Hamiltonian $\mathcal{H}_I^1(t)$,

$$\mathcal{H}_{\rm high}^1(t) = \sum_{n=-\infty,\neq 1}^{+\infty}(-i)^n J_n(\beta_1)g_{1a}|10\rangle\langle 01|e^{i\Delta_1 t}e^{-in(\nu_1 t+\varphi_1)} + {\rm H.c.}, \tag{F1}$$

will cause a deviation in the effective Hamiltonian $\mathcal{H}_L(t)$. We find that the influence extent of these high-order oscillating terms depends on their effective coupling strength $J_n(\beta_1)g_{1a}$ and detuning $(\Delta_1 - n\nu_1)$. Furthermore, the choice of weak coupling strength will reduce the influence of the high-order oscillating terms, but it also induces more decoherence effects due to a longer resulting gate time. Therefore, we need to optimize parameters $\{\beta_1, \Delta_1\}$ to find the result with high gate fidelity. As shown in Figs. 7(a)–7(c), under the fixed coherence time $T_1 = 40\ \mu$s, $T_\phi = 40\ \mu$s, and $T_{\rm res} = 150\ \mu$s, we can determine an optimal parameter region with gate fidelities above 99.90%. The numerical results also verify the competitive contributions between the decoherence and high-order oscillating terms on gate infidelity. So, under the parameters of $\beta_1 \approx 2.1$ and $\Delta_1 = 2\pi \times 180$ MHz considered in the main text, the infidelities of the geometric Hadamard gate, phase gate, and $\pi/8$ gate induced by the decoherence and high-order oscillating terms are about (0.03%, 0.02%), (0.05%, 0.03%), and (0.04%, 0.02%), respectively, with the corresponding gate durations about 14, 27, and 20 ns.

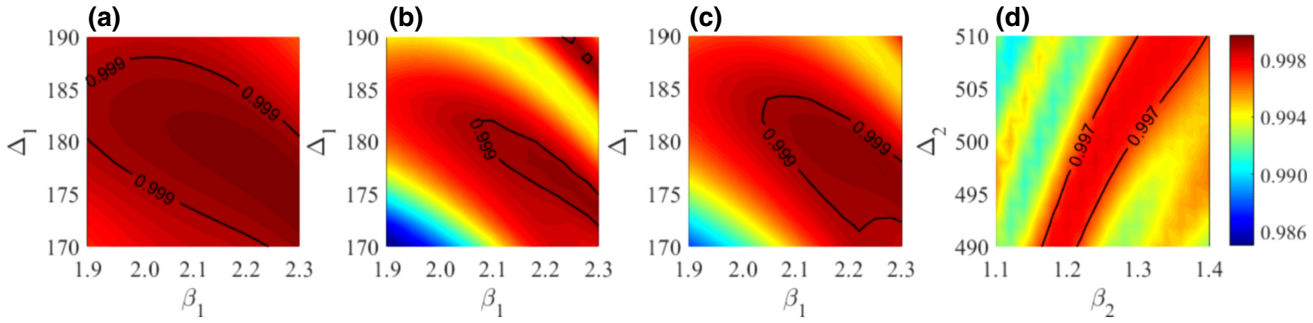

FIG. 7. Gate fidelities of the implemented (a) Hadamard gate, (b) phase gate, (c) $\pi/8$ gate, and (d) controlled-phase gate as functions of tunable parameters.

However, different from the single-logical-qubit case, the high-order oscillating terms in the two-logical-qubit manipulation, $\mathcal{H}^{2}_{\rm high}(t) = \mathcal{H}^{2,1}_{\rm high}(t) + \mathcal{H}^{2,1}_{\rm high}(t)$ with

$$\mathcal{H}^{2,1}_{\rm high}(t) = \sum_{n=-\infty}^{+\infty} (-i)^n J_n(\beta_2) g_{a2} |01\rangle_{a2}\langle 10| e^{i\Delta_2 t} e^{-in(\nu_2 t+\varphi_2)} + \text{H.c.}, \tag{F2}$$

$$\mathcal{H}^{2,2}_{\rm high}(t) = \sum_{n=-\infty,\neq 1}^{+\infty} \sqrt{2}(-i)^n J_n(\beta_2) g_{a2} |02\rangle_{a2}\langle 11| e^{i(\Delta_2-\alpha_2)t} \times e^{-in(\nu_2 t+\varphi_2)} + \sum_{m=-\infty}^{+\infty} \sqrt{2}(-i)^m J_m(\beta_2) g_{a2} |11\rangle_{a2}\langle 20| e^{i\Delta_2 t} \times e^{-im(\nu_2 t+\varphi_2)} + \text{H.c.}, \tag{F3}$$

include not only the parasitic XY coupling $\mathcal{H}^{2,1}_{\rm high}(t)$ between $|01\rangle_{a2}$ and $|10\rangle_{a2}$, but also the various couplings $\mathcal{H}^{2,2}_{\rm high}(t)$ between high-energy levels $|11\rangle_{a2}$ and $|02\rangle_{a2}$, $|20\rangle_{a2}$ that produce the parasitic ZZ crosstalk. It is clear that the influence extent of these high-order oscillating terms depends on the effective coupling strength $J_{n,m}(\beta_2)g_{a2}$ and effective detuning associated with Δ_2. In the same way, consider the competitive contributions between the decoherence and high-order oscillating terms on gate infidelity; here we also need to optimize parameters $\{\beta_2, \Delta_2\}$ to find the result with high gate fidelity. As shown in Fig. 7(d), we can determine an optimal parameter region with gate fidelities above 99.70%. Furthermore, by analyzing the numerical simulation results, at parameters $\beta_2 \approx 1.2$ and $\Delta_2 = 2\pi \times 500$ MHz considered in the main text, the infidelities of the two-logical-qubit controlled-phase geometric gate induced by decoherence and high-order oscillating terms are about (0.18%, 0.06%) with the corresponding gate duration about 55 ns. Thus, it can be seen that the influence of the parasitic XY coupling and ZZ crosstalk on gate performance can be suppressed to a low level in the optimal parameter region, contributing to gate infidelities of about 0.02% and 0.04%, respectively.

Finally, both in our single- and two-logical-qubit manipulations, to suppress unwanted coupling with neighboring qubits induced by the drive signal in a realistic device, we need to tune the frequencies of neighboring qubits to be initially detuned with our physical qubits used for encoding. We have numerically verified that, when the qubit-frequency difference between neighboring qubits and our physical qubits used for encoding is larger than $2\pi \times 1$ GHz, the gate infidelity that results from the unwanted coupling with neighboring qubits will be less than 0.01%, and thus can be ignored here.

[1] M. A. Nielsen and I. L. Chuang, *Quantum Computation and Quantum Information* (Cambridge University Press, Cambridge, 2000).
[2] M. V. Berry, Quantal phase factors accompanying adiabatic changes, Proc. R. Soc. London A **392**, 45 (1984).
[3] F. Wilczek and A. Zee, Appearance of Gauge Structure in Simple Dynamical Systems, Phys. Rev. Lett. **52**, 2111 (1984).
[4] Y. Aharonov and J. Anandan, Phase Change During a Cyclic Quantum Evolution, Phys. Rev. Lett. **58**, 1593 (1987).
[5] J. Samuel and R. Bhandari, General Setting for Berry's Phase, Phys. Rev. Lett. **60**, 2339 (1988).
[6] P. Zanardi and M. Rasetti, Holonomic quantum computation, Phys. Lett. A **264**, 94 (1999).
[7] J. Pachos, P. Zanardi, and M. Rasetti, Non-Abelian Berry connections for quantum computation, Phys. Rev. A **61**, 010305(R) (1999).
[8] J. A. Jones, V. Vedral, A. Ekert, and G. Castagnoli, Geometric quantum computation using nuclear magnetic resonance, Nature **403**, 869 (2000).
[9] L.-M. Duan, J. I. Cirac, and P. Zoller, Geometric manipulation of trapped ions for quantum computation, Science **292**, 1695 (2001).
[10] L. Faoro, J. Siewert, and R. Fazio, Non-Abelian Holonomies, Charge Pumping, and Quantum Computation

with Josephson Junctions, Phys. Rev. Lett. **90**, 028301 (2003).
[11] W. Xiang-Bin and M. Keiji, Nonadiabatic Conditional Geometric Phase Shift with NMR, Phys. Rev. Lett. **87**, 097901 (2001).
[12] S.-L. Zhu and Z. D. Wang, Implementation of Universal Quantum Gates Based on Nonadiabatic Geometric Phases, Phys. Rev. Lett. **89**, 097902 (2002).
[13] S.-L. Zhu and Z. D. Wang, Unconventional Geometric Quantum Computation, Phys. Rev. Lett. **91**, 187902 (2003).
[14] E. Sjöqvist, D. M. Tong, L. M. Andersson, B. Hessmo, M. Johansson, and K. Singh, Non-adiabatic holonomic quantum computation, New J. Phys. **14**, 103035 (2012).
[15] P. Z. Zhao, X. D. Cui, G. F. Xu, E. Sjöqvist, and D. M. Tong, Rydberg-atom-based scheme of nonadiabatic geometric quantum computation, Phys. Rev. A **96**, 052316 (2017).
[16] T. Chen and Z.-Y. Xue, Nonadiabatic Geometric Quantum Computation with Parametrically Coupled Transmons, Phys. Rev. Appl. **10**, 054051 (2018).
[17] W. Dong, F. Zhuang, S. E. Economou, and E. Barnes, Doubly Geometric Quantum Control, PRX Quantum **2**, 030333 (2021).
[18] D. Leibfried, B. DeMarco, V. Meyer, D. Lucas, M. Barrett, J. Britton, W. M. Itano, B. Jelenković, C. Langer, T. Rosenband, and D. J. Wineland, Experimental demonstration of a robust, high-fidelity geometric two ion-qubit phase gate, Nature (London) **422**, 412 (2003).
[19] M.-Z. Ai, S. Li, Z. Hou, R. He, Z.-H. Qian, Z.-Y. Xue, J.-M. Cui, Y.-F. Huang, C.-F. Li, and G.-C. Guo, Experimental Realization of Nonadiabatic Holonomic Single-Qubit Quantum Gates with Optimal Control in a Trapped Ion, Phys. Rev. Appl. **14**, 054062 (2020).
[20] J. Du, P. Zou, and Z. D. Wang, Experimental implementation of high-fidelity unconventional geometric quantum gates using an NMR interferometer, Phys. Rev. A **74**, 020302(R) (2006).
[21] G. Feng, G. Xu, and G. Long, Experimental Realization of Nonadiabatic Holonomic Quantum Computation, Phys. Rev. Lett. **110**, 190501 (2013).
[22] H. Li, Y. Liu, and G. Long, Experimental realization of single-shot nonadiabatic holonomic gates in nuclear spins, Sci. China-Phys. Mech. Astron. **60**, 080311 (2017).
[23] Z. Zhu, T. Chen, X. Yang, J. Bian, Z.-Y. Xue, and X. Peng, Single-Loop and Composite-Loop Realization of Nonadiabatic Holonomic Quantum Gates in a Decoherence-Free Subspace, Phys. Rev. Appl. **12**, 024024 (2019).
[24] A. A. Abdumalikov, J. M. Fink, K. Juliusson, M. Pechal, S. Berger, A. Wallraff, and S. Filipp, Experimental realization of non-Abelian non-adiabatic geometric gates, Nature (London) **496**, 482 (2013).
[25] Y. Xu, W. Cai, Y. Ma, X. Mu, L. Hu, T. Chen, H. Wang, Y. P. Song, Z.-Y. Xue, Z.-Q. Yin, and L. Sun, Single-Loop Realization of Arbitrary Nonadiabatic Holonomic Single-Qubit Quantum Gates in a Superconducting Circuit, Phys. Rev. Lett. **121**, 110501 (2018).
[26] D. J. Egger, M. Ganzhorn, G. Salis, A. Fuhrer, P. Müller, P. K. Barkoutsos, N. Moll, I. Tavernelli, and S. Filipp, Entanglement Generation in Superconducting Qubits Using Holonomic Operations, Phys. Rev. Appl. **11**, 014017 (2019).
[27] T. Yan, B.-J. Liu, K. Xu, C. Song, S. Liu, Z. Zhang, H. Deng, Z. Yan, H. Rong, K. Huang, M.-H. Yung, Y. Chen, and D. Yu, Experimental Realization of Nonadiabatic Shortcut to Non-Abelian Geometric Gates, Phys. Rev. Lett. **122**, 080501 (2019).
[28] Y. Xu, Z. Hua, T. Chen, X. Pan, X. Li, J. Han, W. Cai, Y. Ma, H. Wang, Y. Song, Z.-Y. Xue, and L. Sun, Experimental Implementation of Universal Nonadiabatic Geometric Quantum Gates in a Superconducting Circuit, Phys. Rev. Lett. **124**, 230503 (2020).
[29] P. Z. Zhao, Z. Dong, Z. Zhang, G. Guo, D. M. Tong, and Y. Yin, Experimental realization of nonadiabatic geometric gates with a superconducting Xmon qubit, Sci. China-Phys. Mech. Astron. **64**, 250362 (2021).
[30] K. Xu, W. Ning, X.-J. Huang, P.-R. Han, H. Li, Z.-B. Yang, D. Zheng, H. Fan, and S.-B. Zheng, Demonstration of a non-Abelian geometric controlled-NOT gate in a superconducting circuit, Optica **8**, 972 (2021).
[31] C. Zu, W.-B. Wang, L. He, W.-G. Zhang, C.-Y. Dai, F. Wang, and L.-M. Duan, Experimental realization of universal geometric quantum gates with solid-state spins, Nature (London) **514**, 72 (2014).
[32] S. Arroyo-Camejo, A. Lazariev, S. W. Hell, and G. Balasubramanian, Room temperature high-fidelity holonomic single-qubit gate on a solid-state spin, Nat. Commun. **5**, 4870 (2014).
[33] Y. Sekiguchi, N. Niikura, R. Kuroiwa, H. Kano, and H. Kosaka, Optical holonomic single quantum gates with a geometric spin under a zero field, Nat. Photon. **11**, 309 (2017).
[34] B. B. Zhou, P. C. Jerger, V. O. Shkolnikov, F. J. Heremans, G. Burkard, and D. D. Awschalom, Holonomic Quantum Control by Coherent Optical Excitation in Diamond, Phys. Rev. Lett. **119**, 140503 (2017).
[35] K. Nagata, K. Kuramitani, Y. Sekiguchi, and H. Kosaka, Universal holonomic quantum gates over geometric spin qubits with polarised microwaves, Nat. Commun. **9**, 3227 (2018).
[36] Y. Dong, S.-C. Zhang, Y. Zheng, H.-B. Lin, L.-K. Shan, X.-D. Chen, W. Zhu, G.-Z. Wang, G.-C. Guo, and F.-W. Sun, Experimental Implementation of Universal Holonomic Quantum Computation on Solid-State Spins with Optimal Control, Phys. Rev. Appl. **16**, 024060 (2021).
[37] Y. Ota and Y. Kondo, Composite pulses in NMR as nonadiabatic geometric quantum gates, Phys. Rev. A **80**, 024302 (2009).
[38] J. Zhou, S. Li, G.-Z. Pan, G. Zhang, T. Chen, and Z.-Y. Xue, Nonadiabatic geometric quantum gates that are insensitive to qubit-frequency drifts, Phys. Rev. A **103**, 032609 (2021).
[39] G. F. Xu and G. L. Long, Protecting geometric gates by dynamical decoupling, Phys. Rev. A **90**, 022323 (2014).
[40] X. Wu and P. Z. Zhao, Universal nonadiabatic geometric gates protected by dynamical decoupling, Phys. Rev. A **102**, 032627 (2020).
[41] T. Chen and Z.-Y. Xue, High-Fidelity and Robust Geometric Quantum Gates that Outperform Dynamical Ones, Phys. Rev. Appl. **14**, 064009 (2020).
[42] C.-Y. Ding, L.-N. Ji, T. Chen, and Z.-Y. Xue, Path-optimized nonadiabatic geometric quantum computation on

superconducting qubits, Quantum Sci. Technol. **7**, 015012 (2022).
[43] L.-M. Duan and G.-C. Guo, Preserving Coherence in Quantum Computation by Pairing Quantum Bits, Phys. Rev. Lett. **79**, 1953 (1997).
[44] P. Zanardi and M. Rasetti, Noiseless Quantum Codes, Phys. Rev. Lett. **79**, 3306 (1997).
[45] D. A. Lidar, I. L. Chuang, and K. B. Whaley, Decoherence-Free Subspaces for Quantum Computation, Phys. Rev. Lett. **81**, 2594 (1998).
[46] P. G. Kwiat, A. J. Berglund, J. B. Altepeter, and A. G. White, Experimental verification of decoherence-free subspaces, Science **290**, 498 (2000).
[47] L. A. Wu, P. Zanardi, and D. A. Lidar, Holonomic Quantum Computation in Decoherence-Free Subspaces, Phys. Rev. Lett. **95**, 130501 (2005).
[48] L. X. Cen, Z. D. Wang, and S. J. Wang, Scalable quantum computation in decoherence-free subspaces with trapped ions, Phys. Rev. A **74**, 032321 (2006).
[49] X. L. Feng, C. F. Wu, H. Sun, and C. H. Oh, Geometric Entangling Gates in Decoherence-Free Subspaces with Minimal Requirements, Phys. Rev. Lett. **103**, 200501 (2009).
[50] G. F. Xu, J. Zhang, D. M. Tong, E. Sjöqvist, and L. C. Kwek, Nonadiabatic Holonomic Quantum Computation in Decoherence-Free Subspaces, Phys. Rev. Lett. **109**, 170501 (2012).
[51] J. Zhang, L.-C. Kwek, E. Sjöqvist, D. M. Tong, and P. Zanardi, Quantum computation in noiseless subsystems with fast non-Abelian holonomies, Phys. Rev. A **89**, 042302 (2014).
[52] Z.-Y. Xue, J. Zhou, and Z. D. Wang, Universal holonomic quantum gates in decoherence-free subspace on superconducting circuits, Phys. Rev. A **92**, 022320 (2015).
[53] P. Z. Zhao, G. F. Xu, and D. M. Tong, Nonadiabatic geometric quantum computation in decoherence-free subspaces based on unconventional geometric phases, Phys. Rev. A **94**, 062327 (2016).
[54] T. Chen, P. Shen, and Z.-Y. Xue, Robust and Fast Holonomic Quantum Gates with Encoding on Superconducting Circuits, Phys. Rev. Appl. **14**, 034038 (2020).
[55] F. Motzoi, J. M. Gambetta, P. Rebentrost, and F. K. Wilhelm, Simple Pulses for Elimination of Leakage in Weakly Nonlinear Qubits, Phys. Rev. Lett. **103**, 110501 (2009).
[56] Z. Chen, J. Kelly, C. Quintana, R. Barends, B. Campbell, Y. Chen, B. Chiaro, A. Dunsworth, A. G. Fowler, and E. Lucero, *et al.*, Measuring and Suppressing Quantum State Leakage in a Superconducting Qubit, Phys. Rev. Lett. **116**, 020501 (2016).
[57] J. D. Strand, M. Ware, F. Beaudoin, T. A. Ohki, B. R. Johnson, A. Blais, and B. L. T. Plourde, First-order sideband transitions with flux-driven asymmetric transmon qubits, Phys. Rev. B **87**, 220505 (2013).
[58] M. Reagor, C. B. Osborn, N. Tezak, A. Staley, G. Prawiroatmodjo, M. Scheer, N. Alidoust, E. A. Sete, N. Didier, and M. P. da Silva, *et al.*, Demonstration of universal parametric entangling gates on a multi-qubit lattice, Sci. Adv. **4**, eaao3603 (2018).
[59] R. Barends, J. Kelly, A. Megrant, A. Veitia, D. Sank, E. Jeffrey, T. C. White, J. Mutus, A. G. Fowler, and B. Campbell, *et al.*, Superconducting quantum circuits at the surface code threshold for fault tolerance, Nature (London) **508**, 500 (2014).
[60] R. W. Heeres, P. Reinhold, N. Ofek, L. Frunzio, L. Jiang, M. H. Devoret, and R. J. Schoelkopf, Implementing a universal gate set on a logical qubit encoded in an oscillator, Nat. Commun. **8**, 94 (2017).
[61] L. Hu, Y. Ma, W. Cai, X. Mu, Y. Xu, W. Wang, Y. Wu, H. Wang, Y. P. Song, C.-L. Zou, S. M. Girvin, L-M. Duan, and L. Sun, Quantum error correction and universal gate set operation on a binomial bosonic logical qubit, Nat. Phys. **15**, 503 (2019).
[62] P. Krantz, M. Kjaergaard, F. Yan, T. P. Orlando, S. Gustavsson, and W. D. Oliver, A quantum engineer's guide to superconducting qubits, Appl. Phys. Rev. **6**, 021318 (2019).
[63] N. Didier, E. A. Sete, J. Combes, and M. P. da Silva, ac Flux Sweet Spots in Parametrically Modulated Superconducting Qubits, Phys. Rev. Appl. **12**, 054015 (2019).
[64] Z. Huang, P. S. Mundada, A. Gyenis, D. I. Schuster, A. A. Houck, and J. Koch, Engineering Dynamical Sweet Spots to Protect Qubits from $1/f$ Noise, Phys. Rev. Appl. **15**, 034065 (2021).
[65] S.-B. Zheng, C.-P. Yang, and F. Nori, Comparison of the sensitivity to systematic errors between nonadiabatic non-Abelian geometric gates and their dynamical counterparts, Phys. Rev. A **93**, 032313 (2016).